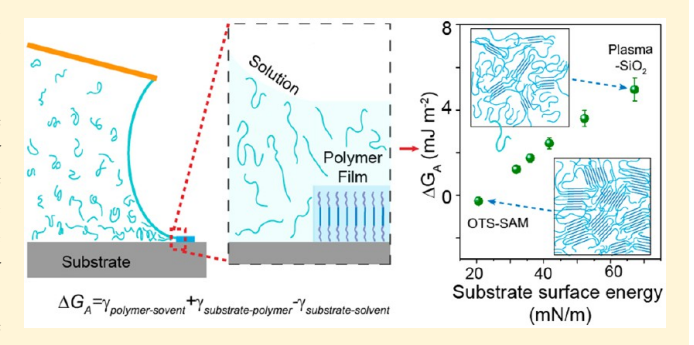
Critical Role of Surface Energy in Guiding Crystallization of Solution-Coated Conjugated Polymer Thin Films

Fengjiao Zhang,^{†, ||} Erfan Mohammadi,^{†, ||} Xuyi Luo,[‡] Joseph Strzalka,[§] Jianguo Mei,[‡] and Ying Diao*,[†]

Supporting Information

ABSTRACT: It is well-known that substrate surface properties have a profound impact on the morphology of thin films solution coated atop and the resulting solid-state properties. However, design rules for guiding the substrate selection have not yet been established. Such design rules are particularly important for solution-coated semiconducting polymers, as the substrate-directed thin film morphology can impact charge transport properties by orders of magnitude. We hypothesize that substrate surface energies dictate the thin film morphology by modulating the free energy barrier to heterogeneous nucleation. To test this hypothesis, we systematically vary the substrate surface energy via surface functionalization techni-



ques. We perform in-depth morphology and device characterizations to establish the relationship between substrate surface energy, thin film morphology and charge transport properties, employing donor—acceptor (D—A) conjugated polymers. We find that decreasing the substrate surface energy progressively increases thin film crystallinity, degree of molecular ordering, and extent of domain alignment. Notably, the enhanced morphology on the lowest surface energy substrate leads to a 10-fold increase in the charge carrier mobility. We further develop a free energy model relating the substrate surface energy to the penalty of heterogeneous nucleation from solution in the thin film geometry. The model correctly predicts the experimental trend, thereby validating our hypothesis. This work is a significant step toward establishing design rules and understanding the critical role of substrates in determining morphology of solution-coated thin films.

1. INTRODUCTION

The morphology of organic semiconductor (OSC) thin films, from molecular conformation and crystal packing, degree of (para)crystallinity and percolation, to domain size and orientation ordering, is critical to their electronic performance, in particular charge carrier mobilities. Many strategies for modulating the OSC thin film morphology have been developed, summarized in several recent reviews covering both small molecule and polymer semiconductors. In particular, substrate surface properties such as hydrophobicity, polarity, and nanoscale topology have been under intense investigations toward understanding their relationship with thin film morphology and charge transport properties.

Early on, many studies have observed pronounced modulation of out-of-plane molecular orientation of OSCs by surface treatment of the dielectric layer. ^{30,35–39} For instance, Toney and co-workers found that octadecyltrichlorosilane (OTS) treated SiO₂ substrate yielded a preferred out-of-plane orientation of poly(3-hexylthiophene) (P3HT) crystallites compared to misoriented crystallites on hexamethyldisilazane (HMDS) treated substrates. ³⁵ Cho and co-workers separately discovered that P3HT adopted "edge-on" orientation on amine

SAMs, in contrast to "face-on" orientation on alkyl SAMs. They further rationalized that the repulsive interaction between amine lone pair electrons and the thienyl moieties in P3HT backbone led to "edge-on" stacking, while the π -H interactions between P3HT and alkyl SAMs resulted in "face-on" stacking. Tokito et al. established a quantitative relationship between the substrate surface energies and the hole mobility of poly(2,5-bis(3-hexadecylthiophene-2-yl)thieno[3,2-b]-thiophene) (PB16TTT). They observed the highest mobility reaching 1 cm²/(V s) on a fluoroalkyl SAM with a low surface energy of 13.3 mN/m. However, the substrate surface could alter mobility through both thin film morphology and interfacial trap density. The exact mechanism was not elucidated in this work. In addition to surface chemistry, Hu, Zhen and coauthors recently demonstrated the synergistic

Special Issue: Early Career Authors in Fundamental Colloid and Interface Science

Received: August 9, 2017 Revised: September 29, 2017 Published: October 2, 2017



[†]Department of Chemical and Biomolecular Engineering, University of Illinois at Urbana–Champaign, 600 South Mathews Avenue, Urbana, Illinois 61801, United States

[‡]Department of Chemistry, Purdue University, 560 Oval Drive, West Lafayette, Indiana 47907, United States

[§]X-ray Science Division, Advanced Photon Source, Argonne National Laboratory, Argonne, Illinois 60349, United States

effect of surface nanogrooves and high polarity of poly(amic acid) dielectric on promoting "edge-on" orientation of pentacene.²⁷ They reported that such substrate enabled high device performance (~30 cm²/(V s)) on par with single crystal devices. Apart from molecule orientation, substrates also have a significant impact on the OSC crystal growth kinetics. Loo et al. measured differential crystallization rates of triethylsilylethynyl anthradithiophene (TES-ADT) on substrates of various surface energies during solvent vapor annealing.⁴⁰ They found the existence of an optimum crystal growth rate at an intermediate substrate surface energy, which was then utilized to guide crystallization along arbitrary patterns.

Despite impressive progress on our understanding of substrate-directed thin film crystallization over the past decade, to date, no quantitative design rules exist that can predict the thin film morphology dictated by substrate surface properties. In addition, most studies involving solution processing did not account for the role of solvent in mediating the substrate-OSC interactions. On the other hand, solutes cannot crystallize on a substrate without simultaneously ejecting preadsorbed solvent molecules. In other words, all pairwise interactions between substrate, solute and solvent are expected to govern the crystallization process from solution. 41,42 Furthermore, how substrate-induced crystallization directly correlates with charge transport properties is not always clear, as such effects are frequently compounded with the modulation of interfacial trap density by substrate treatment.

In this work, we tackle these challenges by performing a systematic investigation on surface-induced crystallization of a donor-acceptor (D-A) semiconducting polymer during meniscus-guided coating process, focusing on the role of substrate surface energy. To establish the surface energy-thin film morphology-charge transport property relationship, we performed comprehensive morphology and device characterizations combining cross-polarized optical microscopy (C-POM), UV-vis spectroscopy (UV-vis), atomic force microscopy (AFM), grazing incidence X-ray diffraction (GIXD) and organic field-effect transistor (OFET) device measurements. We further developed a generic free energy model for heterogeneous nucleation in thin films based on the hypothesis that substrate surface energies dictate the thin film morphology by modulating the free energy barrier to heterogeneous nucleation. The model considered all pairwise interfacial free energies between the substrate, the solute and the solvent, which correctly predicted the observed trend in surface-energydependent thin film morphology.

2. EXPERIMENTAL SECTION

Materials. The organic semiconductor (OSC), poly-(diketopyrrolopyrrole-thiophene-thieno[3,2,b]thiophene-thiophene) (DPP2T-TT) ($M_n = 16000 \text{ g mol}^{-1}$), and isoindigo-alt-bithiophene based polymer (PII-2T) ($M_n = 117000 \text{ g mol}^{-1}$) used in this study were synthesized as previous reported. ^{10,43,44} Octadecyltrichlorosilane (OTS), phenyltrichlorosilane (PTS), poly(4-vinylphenol) (PVP, $M_w =$ 25000 g mol⁻¹), cross-linker 4,4'-(hexafluoroisopropylidene)diphthalic anhydride (HDA), and solvent propylene glycol monomethyl ether acetate (PGMEA, ReagentPlus), toluene (Anhydrous), trichloroethylene (ACS grade) and chloroform (Anhydrous) were purchased from Sigma-Aldrich. Pentafluorophenylpropyltrichlorosilane (FPTS, SIP6716.4) was purchased from Gelest. All materials were used as

Substrate Treatment. Thermally grown SiO2, Corning glass, and a heavily doped silicon wafer with native oxide were used as substrates for polymer thin film fabrication. The substrates were rinsed with

toluene, acetone, and isopropanol, and dried with nitrogen gas. Before functionalization with self-assembled monolayers (SAMs) or polymeric thin film coatings, the substrates were treated with oxygen plasma at a power of 30 W for 10 min (plasma cleaner PDC-001, Harrick Plasma, Ithaca, NY). For OTS SAMs, the plasma-treated substrates were immersed in 0.2 v% solution in anhydrous trichloroethylene at room temperature. For PTS, 3 v% solution in anhydrous toluene was used and heated under 90 °C for 12-15 h. For FPTS, the plasma-treated substrates were exposed to FPTS vapor in a vacuum oven kept at 75 $^{\circ}\text{C}$ and 580 Torr for 1 h. For PVP:HDA thin film coatings, the PVP/HDA solution (10:1 by weight, 20 mg/mL for PVP) was prepared in solvent PGMEA. The solution was spin coated on the oxygen plasma-treated substrate at 7000 rpm, and subsequently cured at 100 °C in air for 1 h.

Solution Coating of OSC Thin Films. The meniscus-guided coating method was reported in our previous publications. 5,10, brief, a silicon wafer with OTS-functionalized 300 nm SiO2 was used as the coating blade. The blade was titled by 7°. The gap between the substrate and the blade front was kept as 100 μm . The substrate temperature was set at 25 °C. A DPP2T-TT/chloroform solution was used to deposit OSC films on various substrates, at a printing speed of 0.5 mm/s. The concentration ranged from 3.5-4.5 mg/mL to finetune the thickness of OSC layers to yield comparable film thickness (~30 nm) across all substrates. For the spin-coating process, DPP2T-TT solution (chloroform, 4.0-5.5 mg/mL) was dispensed on various substrates when the spin-coater was operating at a speed of 5000 rpm, 46 resulting in similar film thicknesses of ~30 nm.

Film Morphology Characterizations. As-fabricated DPP2T-TT thin films were visualized using an optical microscope (Nikon Ci-POL) under the cross-polarized light. Asylum Research Cypher (Asylum Research) was used to characterize the surface morphology and thickness of the semiconducting layer. Solid-state transmission UV-vis spectroscopy measurements were carried out on the Agilent Cary 60 UV-vis spectrometer; the incident light was polarized vertically using a broadband sheet polarizer. Grazing-incidence X-ray diffraction (GIXD) was performed at the small-wide-angle X-ray scattering beamline 8-ID-E at the Advanced Photon Source, with an Xray beam energy of 11 keV.⁴⁷ For GIXD measurements, Si substrate with native oxide was used to solution coat DPP2T-TT thin films after surface functionalization. During the measurement, the samples were placed in a helium chamber, with a 228 mm sample-to-detector distance. The incidence angle was 0.14° and the exposure time was 10 s. Each sample was scanned at various in-plane rotation angles (φ) by rotating the substrate with respect to the incidence beam (Figure 4a) by 0° , 30° , 60° , and 90° . Herein, φ is defined as 0° when the film coating direction is oriented parallel to the incident beam. Data analysis was performed with the software GIXSGUI, which includes a correction for the polarization of the synchrotron X-ray beam. 48,49 Partial pole figures were constructed by extracting (010) π – π stacking peak intensities as a function of the polar angle χ (13–88° binned into 5° increments) to analyze domain orientation distribution, as well as relative degree of crystallinity. To accurately calculate the peak intensities, multipeak fitting was performed with Igor Pro on the intensity versus q curve obtained from each 5° segment along the γ axis. The purpose was to deconvolute the π - π stacking peak from the amorphous ring and the background scattering. The peak intensity and area thus obtained were further normalized by the film thickness and beam irradiated area on the films. The background diffractions of all substrates were also carried out under the same condition.

Electrical Property Characterizations. For bottom gate geometry, heavily doped Si wafer with a 300 nm SiO2 layer was used as bottom-gate electrode and dielectric layer, respectively. After surface treatment at various conditions specified above, the DPP2T-TT thin film was deposited via meniscus-guide coating at conditions listed above. The Au source-drain electrodes were thermally evaporated to reach a thickness of 30 nm. For the top-gate devices, poly(methyl methacrylate) (PMMA, k = 3.6, Sigma-Aldrich) of $M_w =$ 120 kg mol⁻¹ was spun on top of the DPP2T-TT film (with top Au source-drain electrodes already deposited) as the dielectric layer, from a solution in *n*-butylacetate (80 mg mL⁻¹, filtered with PTFE syringe

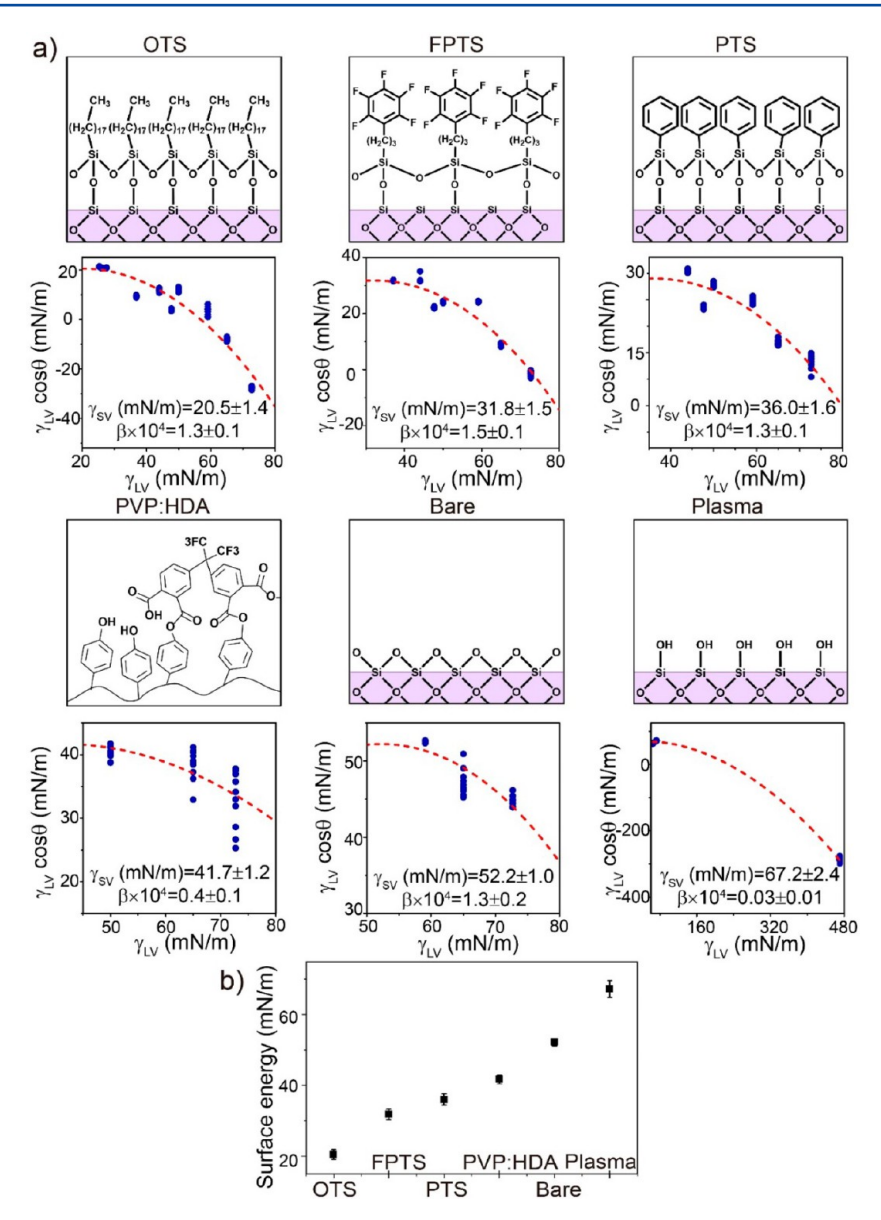


Figure 1. Substrate surface chemistries and surface energies. (a) Schematic illustrating the substrate surface chemistry (top) and corresponding γ_{LV} cos θ versus γ_{LV} graph (bottom). γ_{SV} and β values determined by the two-variable least-squares method from equation-of-state are shown in the inset. (b) Summary of surface energy values for silicon substrates modified with OTS, FPTS, PTS, PVP:HDA, and oxygen plasma.

filter prior to use). After the dielectric deposition, the devices were cured on a hot plate at 100 $^{\circ}$ C for 30 min. The dielectric layer thickness was 480 \pm 10 nm for PMMA. Thereafter, a 40 nm Cu electrode was thermally evaporated through a shadow mask to serve as the top-gate electrode.

The OFET measurements were carried out in a nitrogen environment using a Keysight B1500A analyzer at room temperature. The mobilities calculated in the saturation regime were determined from $I_{\rm DS} = (\mu W C_{\rm ox}/2L)(V_{\rm GS}-V_{\rm T})^2$, where $I_{\rm DS}$ is the source-drain current, μ is the carrier mobility, W and L represent the channel width and length respectively, $C_{\rm ox}$ is the dielectric capacitance per unit area, $V_{\rm GS}$ is the gate voltage and $V_{\rm T}$ is the threshold voltage. The capacitance of PMMA and SiO₂ are 6.3 and 11 nF/cm², respectively.

3. RESULTS AND DISCUSSION

Toward establishing design rules for surface-induced crystallization of OSC thin films, we hypothesize that the substrate surface influences crystallization by modulating the free energy barrier to heterogeneous nucleation, which in turn depends on pairwise intermolecular interactions between the substrate, the

OSC and the solvent. 42 These interactions are embodied in pairwise interfacial free energies, which can be sensitively modulated by varying the substrate surface energy via chemical functionalization. To test this hypothesis, we prepared substrates of a wide range of surface energies by functionalizing silicon wafers with a 300 nm silicon oxide layer using selfassembled monolayers (SAMs), a cross-linked polymer thin film and via oxygen plasma treatment. These functionalized surfaces were chosen considering their direct relevance to organic electronic devices serving as dielectrics layers. The surface chemistries of these substrates are summarized in Figure 1a, and the detailed preparation procedures are described in the Experimental Section. We next quantified their surface energies and determined the surface energy—OSC morphology—charge transport relationship. Based on our hypothesis, we further established a free energy model to unveil the design rule for surface-induced crystallization in OSC thin films.

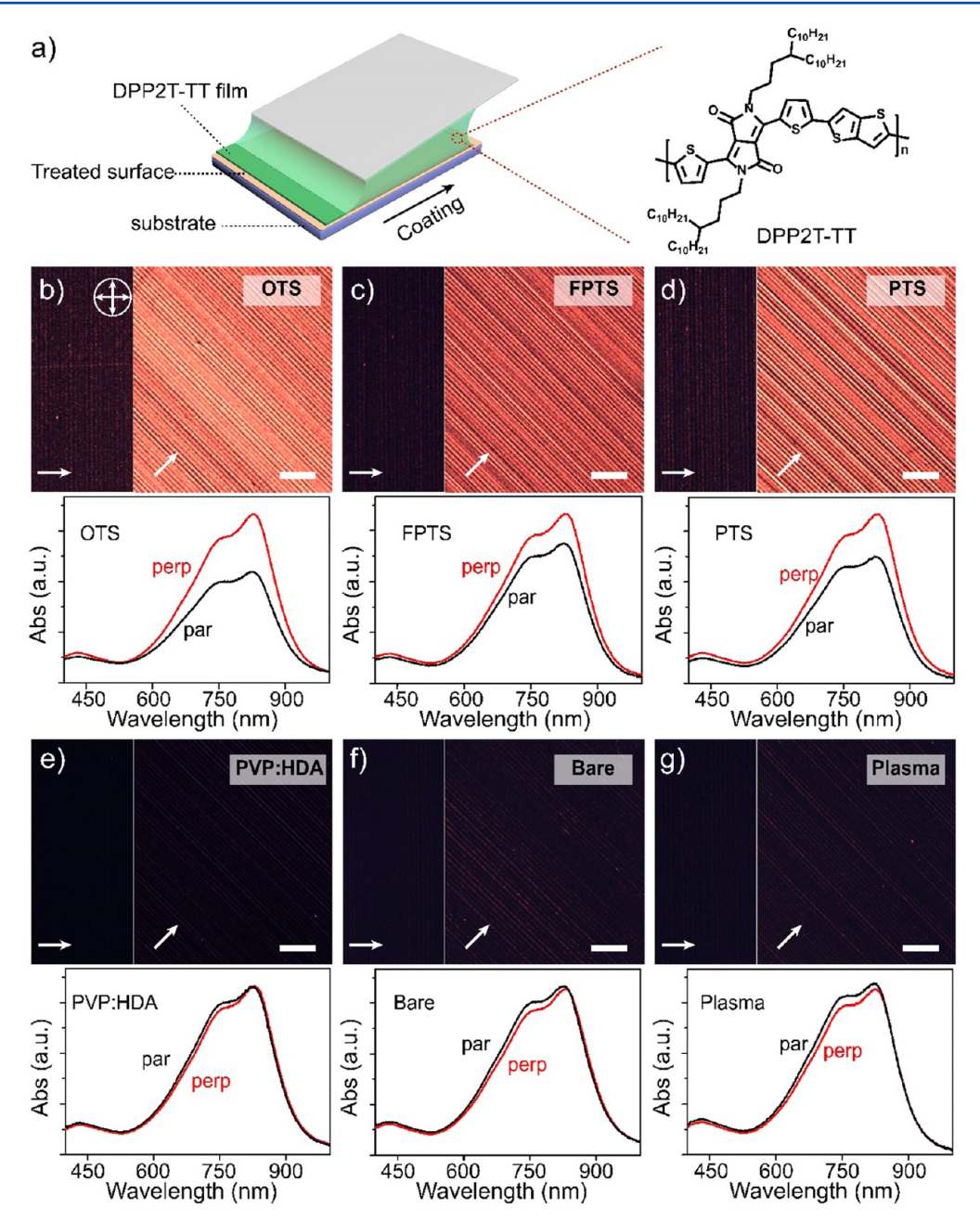


Figure 2. Meniscus-guided coating of DPP2T-TT films on substrates of various surface energies. (a) Schematic of the meniscus-guided coating process and the molecular structure of DPP2T-TT. (b–g) Top: Cross-polarized optical microscopy images of coated DPP2T-TT films on (b) OTS, (c) FPTS, (d) PTS, (e) PVP:HDA, (f) bare, and (g) plasma-treated Si/SiO₂ substrate. Bottom figures are corresponding absorption spectra of polarized UV–vis spectroscopy, where the "par" (black) and "perp" (red) represent the cases when the film coating direction is parallel or perpendicular to the axis of the polarizer. The organic semiconductor layers were of comparable thickness (\sim 30 nm). The orientation of the cross-polarizers is shown on the top left in (b) as crossed arrows, and the white arrows on the bottom left indicate the coating direction. All scale bars are 100 μ m.

3.1. Quantifying Substrate Surface Energies. Several methods have been developed to quantify substrate surface energies, including the commonly employed surface tension component approaches proposed by Fowkes and extended by Owens and Wendt in 1960s^{50,51} and the equation of state approaches originally described by Antonow and Berthelot around 1900,^{52,53} which was later modified by Li and Neumann in 1990.⁵⁴ In this work, we chose the equation of state approach which is theoretically rooted in London theory of dispersion and combining rules.⁵⁵ The modified equation of state by Li and Neumann was shown to be generally applicable,

irrespective of the specific intermolecular interactions involved. Secondomining the equation of state with the Young's equation, the equilibrium contact angle (θ) can be expressed as a function of the substrate surface energy (γ_{SV}) and the probing liquid surface energy (γ_{LV}) , in eq. 1 below (see Supplementary Note and Figure S1 for detailed derivations and discussions):

$$\cos \theta = -1 + 2\sqrt{\frac{\gamma_{\text{SV}}}{\gamma_{\text{LV}}}} \left(1 - \beta(\gamma_{\text{LV}} - \gamma_{\text{SV}})^2\right) \tag{1}$$

wherein β is an empirical constant unique for each substrate, introduced to correct for the deviations from the geometric mean combining rule that underlies the equation of state approach. See Two unknowns, γ_{SV} and β for a specific substrate can be regressed by measuring θ on the substrate using a series of probing liquids with known γ_{LV} . For contact angle measurements, it was shown that θ is best approximated by the quasi-static advancing contact angle, which was measured in this study 56,59 The measurement of θ is sensitive to surface roughness and heterogeneities. In this work, all surfaces were determined to be atomically smooth and chemically homogeneous based on AFM measurements (Figure S2). We selected 10 probing liquids spanning a wide range of molecular structures, intermolecular forces and surface energies (Table S1) to validate that the calculated surface energies are independent of the specific intermolecular interactions as well as to minimize the fitting error. We also made sure that the substrate was practically inert to the probing liquid applied. By plugging in each set of $\gamma_{\rm LV}$ and θ in eq 1, a pair of $\gamma_{\rm SV}$ and β were determined for every substrate from two-variable leastsquares analysis. For data fitting, at least 10 contact angles for each pair of probing liquid and substrate were used to improve the reliability of the regressed γ_{SV} and β and to reduce the fitting error. Conventionally, $\gamma_{\rm LV} \times \cos \theta$ versus $\gamma_{\rm LV}$ curves were plotted to reveal the dependence of $\gamma_{LV} \times \cos \theta$ (and therefore $\gamma_{\rm SV} - \gamma_{\rm SL}$) on $\gamma_{\rm LV}$ following a universal functional form, which formed the basis of the equation of state approach. 60,61 Figure 1a shows the best-fitted $\gamma_{LV} \times \cos \theta$ versus γ_{LV} curves overlaid with the experimental data for each substrate. It can be seen that eq 1 fits the experimental data well, particularly for low surface energy substrates. Note that for high surface energy substrates, the choice of probing liquids becomes limited (Table S2), since high surface energy probing liquids are needed to avoid total wetting conditions when Young's equation is no longer valid. In particular, for plasma-treated substrate, we had to add mercury ($\gamma_{LV} = 470 \text{ mN/m}$) as a probing liquid in addition to glycerol ($\gamma_{LV} = 65.0 \text{ mN/m}$) and water ($\gamma_{LV} = 72.7 \text{ mN/m}$). As a result, higher standard errors were obtained (esp. β) in the cases of higher surface energy substrates.

Using this approach, we determined that the substrate surface energy is successfully modulated over a wide range from 20 to 67 mN/m (Figure 1b). A surface energy of 52.2 mN/m was obtained for the bare silicon substrate without any treatment. SAM modification decreased bare silicon substrate surface energy to 20-37 mN/m, and spin coating a thin layer of PVP:HDA decreased the surface energy to 41.7 mN/m. However, oxygen plasma treatment increased the surface energy to more than 67 mN/m. All calculated substrate surface energies are comparable to, or fall within the range of previously reported values. ^{62,63} Note that the surface energies of bare and plasma-treated silicon substrate may vary from study to study due to differences in fabrication/processing conditions. Therefore, a platform is established to study how systematically changing the substrate surface energy affect conjugated polymer thin film morphology resulted from meniscus-guide coating method (Figure 2a).

3.2. Surface-Induced Thin-Film Morphology. We next investigated the effect of substrate surface energy on morphology of conjugated polymer thin films solution coated atop. A diketopyrrolopyrrole-based D—A conjugated polymer, DPP2T-TT, was selected for this study (Figure 2a); the DPP-based D—A polymers have been intensively investigated due to

their high performance and air stability. 64-66 We deposited DPP2T-TT films from chloroform solution on various substrates via meniscus-guide coating (Figure 2a; see Experimental section). Note that the undulations were found present in all films due to the stick-and-slip motion of the meniscus commonly observed for solution coating in the evaporation regime.^{2,67} To enable direct comparison of morphology and device performance across substrates, we kept the coating speed and substrate temperature the same (0.5) mm/s, 25 °C) and slightly varied solution concentration between 3.5-4.5 mg/mL to obtain the same film thickness (~30 nm) across substrates. The receding contact angles of chloroform on various substrates indicate that the surface energy has minor effect on the ink wetting and drying behavior (Figure S3), allowing us to directly correlate surface energy to observed film morphology. Speed series studies using this material was presented in our previous work.¹⁰

We performed cross-polarized optical microscopy (C-POM) to qualitatively compare the crystallinity and alignment in coated polymer thin films (Figure 2). We observed clear birefringence in the films coated on low surface energy substrates (<40 mN/m), OTS, FPTS, and PTS (Figure 2bd). In contrast, the films coated on high surface energy substrates (>40 mN/m) of PVP:HDA, bare, and plasma-treated silicon wafers were barely birefringent (Figure 2e-g), indicating that these films were of lower degree of crystallinity with crystallite domain sizes too small to detect optically (submicron). The relative degree of crystallinity was further quantified using grazing incidence X-ray diffraction discussed later. Furthermore, for birefringent films, we observed light extinction and the highest birefringence when the coating direction was 0° and 45° with respect to either axis of the crossed polarizers, respectively. This indicates that the conjugated backbone, or the optical transition dipole was preferentially aligned along or transverse to the coating direction (Figure 2b-d).

To determine and quantify the preferential orientation of the backbone, we performed polarized UV-vis spectroscopy to complement the C-POM study (Figure 2b-g). Maximum (minimum) absorption is expected when the transition dipole is aligned with (perpendicular to) the polarizer axis. Although the transition dipole may have the largest component along the long axis of the polymer backbone, the two may not be exactly aligned depending on the backbone curvature. 68,69 Therefore, the UV-vis dichroic ratio only provides a lower bound to the degree of backbone alignment. We observed maximum absorbance when the coating direction was perpendicular to the polarizer axis for films deposited on OTS, FPTS and PTS. This implies that the polymer conjugated backbone is preferentially oriented perpendicular to the coating direction. For films coated on PVP:HDA, bare, and plasma-treated silicon substrates, almost no preferred orientation was observed. Furthermore, the backbone degree of alignment as a function of substrate surface energy was quantified by the dichroic ratio $R = I_{perp}/I_{par}$, defined as the ratio of peak absorbance when the coating direction is perpendicular versus parallel to the polarizer axis (Figure S4). The R values were the highest for films coated on the lowest surface energy substrate, OTS, and exhibited a decreasing trend with increasing substrate surface energy to reach ~1 (isotropic) when the surface energy exceeded 40 mN/m. These observations were consistent with the C-POM results, both pointing to a pronounced and

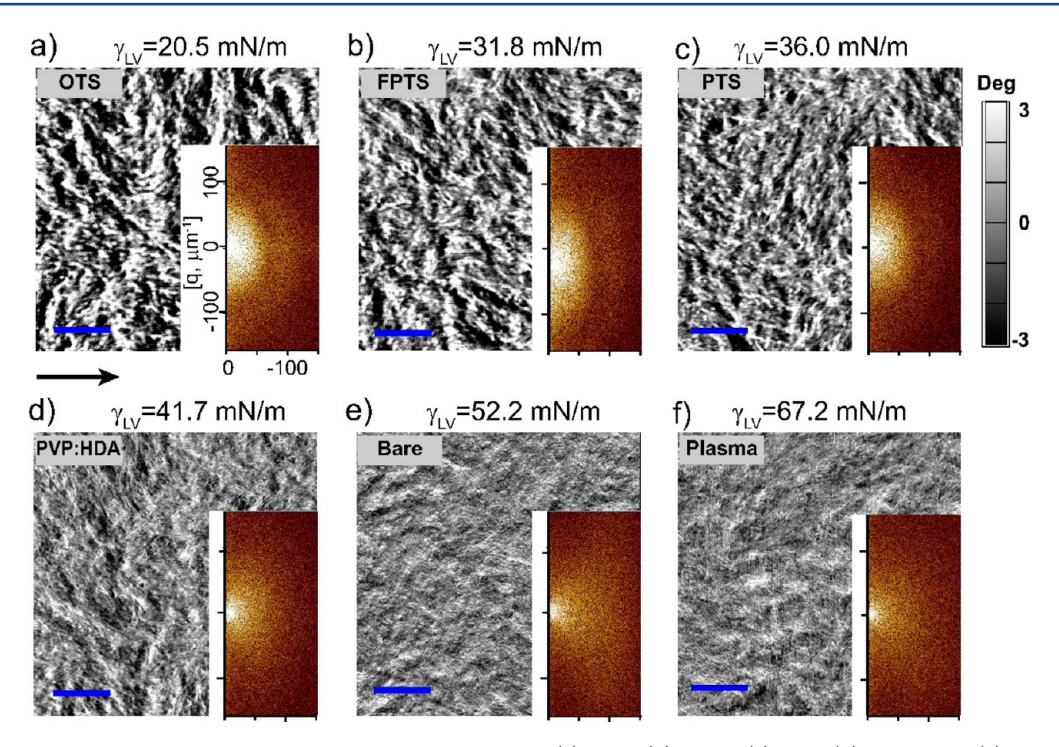


Figure 3. Tapping-mode AFM phase images of DPP2T-TT films coated on (a) OTS, (b) FPTS, (c) PTS, (d) PVP:HDA, (e) bare, and (f) plasmatreated substrate. The scale bars are 0.2 μ m and the arrow denotes the coating direction. The inset figures are the corresponding FFT image.

systematic dependence of film morphology on substrate surface energy.

C-POM and UV-vis measurements yield ensemble-averaged information at the macroscale. We next performed AFM to characterize the mesoscale morphology on the top surface of the films (the interface relevant to charge transport discussed later). AFM phase images showed pronounced fibril-like morphology for low surface energy substrates (Figure 3a-c). Correspondingly, fast Fourier transform (FFT) analysis 5,70 revealed well-defined rings arising from the periodic fibril spacing and narrow fibril size distributions. The uneven distribution of the ring intensity indicated preferential orientation of the fibril long axis perpendicular to the coating direction, consistent with the orientation ordering of the backbone (Figure 2b-d). As the substrate surface energy increased, the ring patterns gradually became diffusive (Figure 3a-c) and eventually diminished when the surface energy increased beyond 40 mN/m (Figure 3d-f), indicating a broad distribution of feature size, morphology, and orientation. Indeed, the fibril-like morphology become less distinctive in the AFM phase images of films on higher surface energy substrates, consistent with the inference from C-POM and UV-vis data.

We next carried out GIXD measurements to characterize the molecular stacking and quantify the relative degree of crystallinity (rDoC) of films coated on various substrates. Given that our solution-coated films are anisotropic in the substrate plane (in-plane) based on UV–vis (Figure 2) and AFM results (Figure 3), we performed GIXD at multiple inplane rotation angles (φ) by rotating the substrate with respect to the incidence beam (Figure 4a) by 0°, 30°, 60°, and 90°. Herein, φ is defined as 0° when the film coating direction is oriented parallel to the incident beam. The background GIXD patterns of blank substrates were shown in Figure S5, and those for OSC thin films were summarized in Figure S6, with representative ones shown in Figure 4b. We define angle χ to

describe the out-of-plane orientation of the π -stacks, with $\chi = 0^{\circ} (90^{\circ})$ representing "face-on" ("edge-on") orientation (Figure 4a,b). Judged from the (010) $\pi - \pi$ stacking peaks, all films exhibited preferential "edge-on" orientation out-of-plane. Integrating the (010) $\pi - \pi$ stacking peak intensity over χ and φ yields the rDoC: 71,72

rDoC
$$\propto \int_0^{\pi/2} \int_0^{\pi/2} \sin(\chi) I(\chi, \varphi) d\chi d\varphi$$
 (2)

We note that variations of eq 2 have been reported for cases when resolution-limited peak is present and when the film is isotropic in-plane (a.k.a. "2D powders"). $^{2,49,71-73}$ To enable comparison of rDoC across various substrates, the peak intensity $I(\chi, \varphi)$ was normalized by the irradiated volume in the thin film (Experimental Section).

In this work, we first present geometrically corrected, normalized $\pi - \pi$ stacking peak intensity, $\sin(\chi) I(\chi, \varphi)$, as a function of χ at each φ = 0°, 30°, 60° and 90°, in order to quantify in-plane anisotropy and alignment. We note that given the geometric constraint of a planar 2D detector, $\chi < 10^{\circ}$ were inaccessible from GIXD scans, and therefore the low χ region close to 0° was not considered in our analysis. Shown in Figure 4c, for the films deposited on low surface energy substrates (OTS, FPTS, and PTS), the population of edge-on π -stacks sharply increased from $\varphi = 0^{\circ}$ to $\varphi = 90^{\circ}$, indicating that the π - π stacking direction preferentially aligned along coating. Equivalently, the polymer backbone favorably oriented perpendicular to coating, consistent with the UV-vis results. We further define a GIXD dichroic ratio R as the ratio of the "edge-on" (83° < χ < 88°) π – π stacking peak areas at φ = 90° versus 0°. The dichroic ratio reached 5.2 for films on the OTS substrate and decreased as the substrate surface energy increased to become almost isotropic $(R \sim 1)$ for films coated on high surface energy substrates (Figure 4d), corroborating the C-POM, UV-vis, and AFM results. Accompanying the

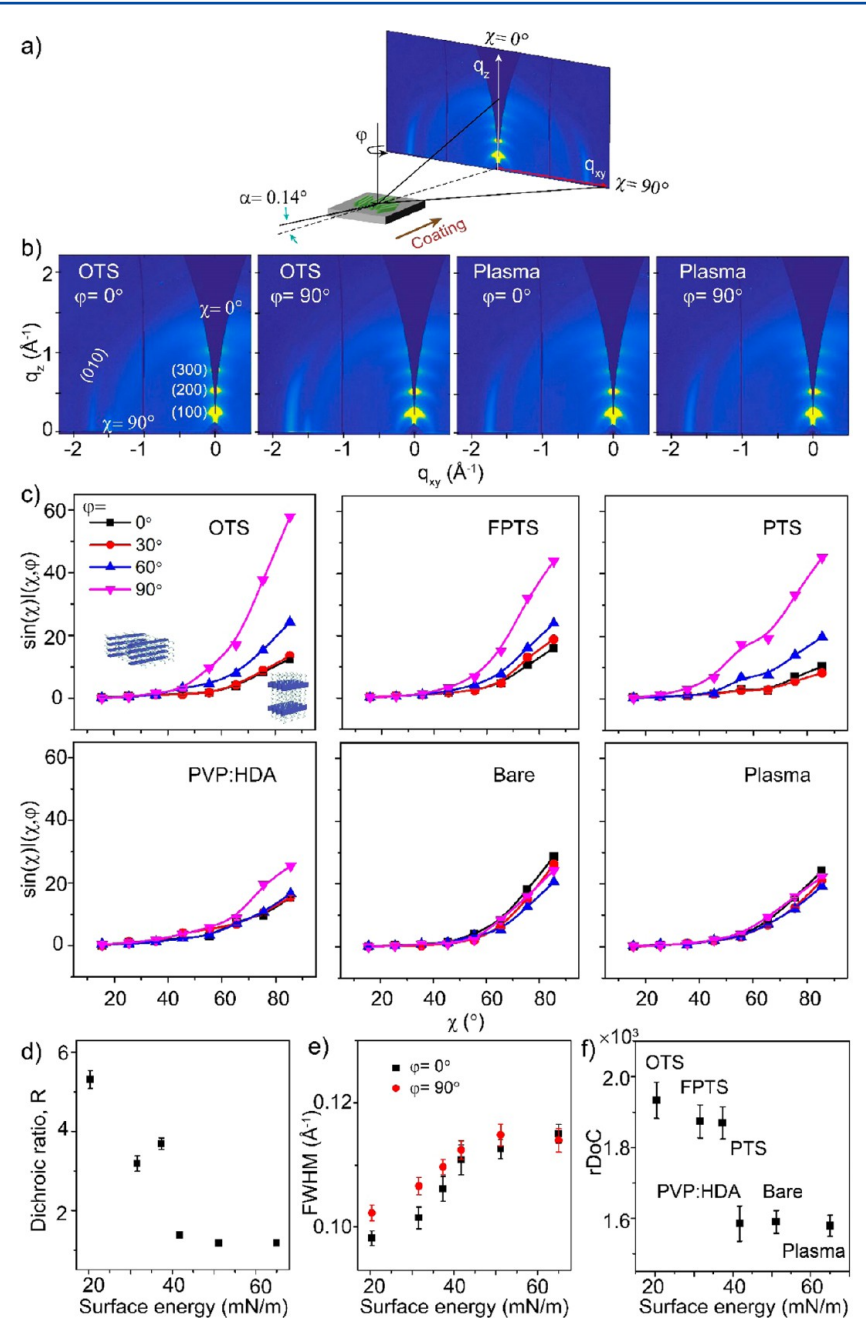


Figure 4. GIXD analysis of polymer thin films coated on various substrates. (a) Configuration of GIXD experiments with a two-dimensional image plate detector. α is the incident angle; φ is the in-plane rotation angle of the substrate, with $\varphi=0^\circ$ when the incidence beam is parallel to the coating direction (as drawn); polar angle χ denotes the out-of-plane orientation of the π -stacks, with $\chi=0^\circ$ representing "face-on" orientation with respect to the substrate plane. (b) GIXD images of thin films coated on OTS versus plasma-treated Si substrates, at $\varphi=0^\circ$ and 90° . (c) Comparison of geometrically corrected intensity of (010) $\pi-\pi$ stacking peak as a function of χ and φ on various substrates. The measurements were taken at $\varphi=0^\circ$ (parallel), 30° , 60° , and 90° (perpendicular) with respect to the incident beam. The error bars represent standard errors of (010) peak areas from multipeak fitting. (d-e) GIXD peak analysis for (d) dichroic ratio and (e) fwhm of "edge-on" $\pi-\pi$ stacking peak for DPP2T-TT polymer thin films dependent on the substrate surface energy. Path length corrected intensity was obtained from a sector cut on GIXD image with $-88^\circ < \chi < -83^\circ$ at $\varphi=0^\circ$ and $\varphi=90^\circ$. Dichroic ratio was calculated as $R=A_\perp/A_\parallel$, where A_\perp and A_\parallel represent the normalized edge-on $\pi-\pi$ stacking peak area with the incident beam perpendicular ($\varphi=90^\circ$) and parallel ($\varphi=0^\circ$) to the coating direction, respectively. (f) Dependence of rDoC on substrate surface energy. The rDoC was estimated according to eq 2.

decaying dichroic ratio is an increasing trend of full width at half-maximum (FWHM) of the same $\pi-\pi$ stacking peaks (Figure 4e). This indicates loss of crystalline order and/or shrinking domain size of the π stacks, concurrent with loss of in-plane orientational ordering with the increase of substrate surface energy. It should be noted that the GIXD dichroic ratio is significantly higher than that of the UV-vis, as GIXD

anisotropy as applied in this work specifically measures edge-on crystallites, whereas UV—vis anisotropy accounts for crystallites with all orientations as well as amorphous domains. Furthermore, UV—vis anisotropy only provides a lower bound as discussed above.

We next estimated rDoC by integrating $\sin(\chi) I(\chi, \varphi)$ over χ and φ . As we scanned limited number of φ angles, full

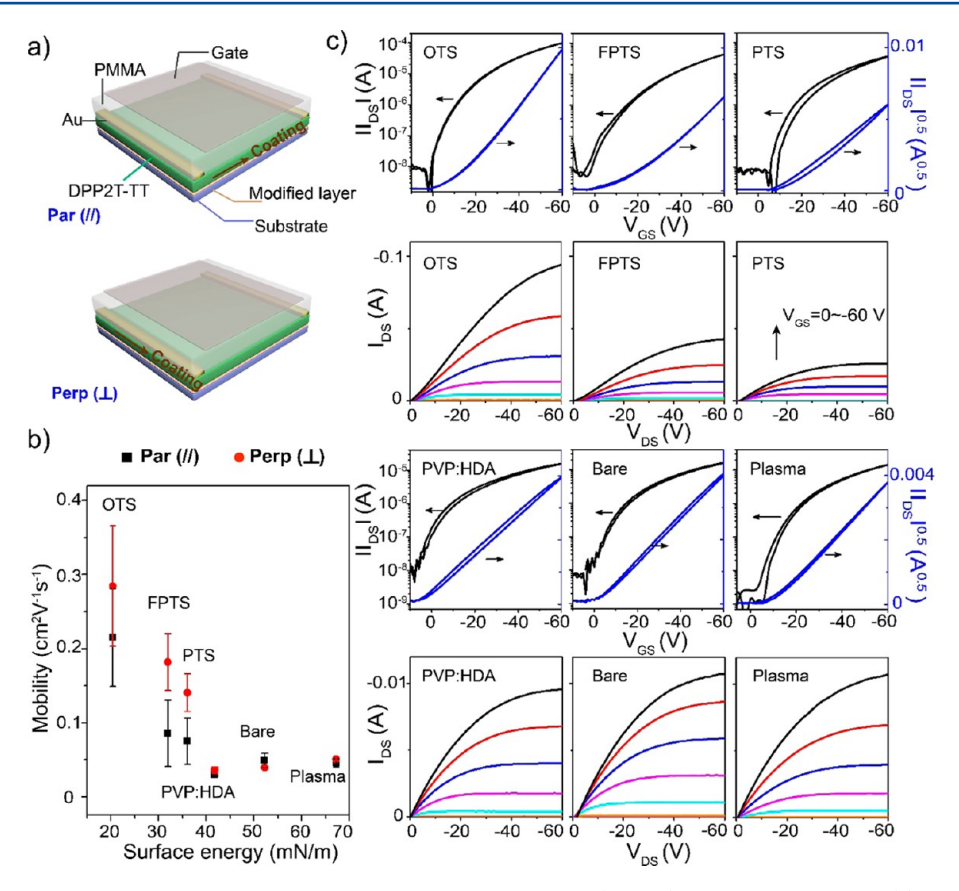


Figure 5. Charge transport property characterizations using top gate, top contact (TGTC) DPP2T-TT OFETs. (a) Schematic of the device architecture for TGTC OFETs constructed, when the conductive channel is parallel (\parallel) or perpendicular (\perp) to the coating direction. (b) Surface energy dependent hole mobility extracted from saturation regime at $V_{\rm DS}$ = $-60~\rm V$. (c) Representative transfer and output curves for devices prepared on various substrates. The conductive channel is perpendicular to the coating direction.

integration was crudely approximated by partial integration over χ and summation over φ instead. We deem this approximation sufficient for capturing the trend of rDoC across substrate surface energies. Shown in Figure 4f, films coated on OTS yielded the highest rDoC, which slightly decreased for films coated on FPTS and PTS before abruptly dropping for films coated on PVP:HDA, bare, and plasmatreated substrates. This result clearly shows the sensitive dependence of crystallization and degree of crystallinity in polymer thin films on substrate surface energy.

3.3. Thin-Film Transistor Characterizations. To establish the substrate-morphology-charge transport relationship, we fabricated top-gate top-contact (TGTC) OFET devices, by thermally evaporating 30 nm Au source/drain electrodes on solution coated DPP2T-TT thin films, followed by spin coating 480 ± 10 nm PMMA dielectric and evaporating 40 nm Cu gate electrode (Figure 5a). Top gate device configuration was chosen such that the dielectric layer is the same across all conditions, eliminating the substrate's impact on charge transport (esp. interfacial trap density being dependent on substrate surface chemistry). This allows us to directly correlate changes in charge transport properties to variations in thin film morphology. The apparent mobilities of TGTC OFETs measured parallel and perpendicular to the coating direction comparing films deposited on different substrates are summarized in Figure 5b. Corresponding transfer, output curves, gate voltage dependent mobilities in the saturation and linear regimes are shown in Figure 5c, Figure S7 and Figure S8. We observed nearly ideal transfer curves with very low

hysteresis. Among devices fabricated on various substrates, OFETs on OTS exhibited the highest average apparent mobility values of 0.22 and 0.29 cm²V⁻¹s⁻¹ for parallel (μ_{\parallel}) and perpendicular (μ_{\perp}) directions, respectively. The slightly higher μ_{\perp} over μ_{\parallel} was attributed to a moderate degree of inplane anisotropy of the polymer backbone and π -stacks observed. We note that no particular effort was spent on optimizing the device performance, and that our mobility values cannot be directly compared with literature values as the side chain structure and the device configuration are different. 64,66,74,75 As the surface energy increased, mobilities gradually decreased by an order of magnitude to 0.03 ± 0.01 cm²V⁻¹s⁻¹ for PVP:HDA substrates and maintained around this value as the surface energy further increased. Interestingly, such a dramatic change in charge carrier mobility was brought by only mild decrease in rDoC (~20%) and loss of moderate inplane alignment (UV-vis dichroic ratio from 1.6 to ~1; GIXD dichroic ratio from 5.2 to ~ 1). These results highlight the sensitive modulation of charge carrier mobility by thin film morphology and the critical role of the substrate surface energy in determining charge transport properties through tuning thin film morphology.

Additionally, we studied the bottom-gate top-contact (BGTC) devices for comparison, which is the most commonly employed device architecture reported in the literature. We observed nonideal transfer curves in almost all cases, exhibiting "kink" features and corresponding spikes in mobility– $V_{\rm GS}$ curves (Figure S9) not present in TGTC devices (Figure Sc and Figure S7). This phenomenon may arise from charge

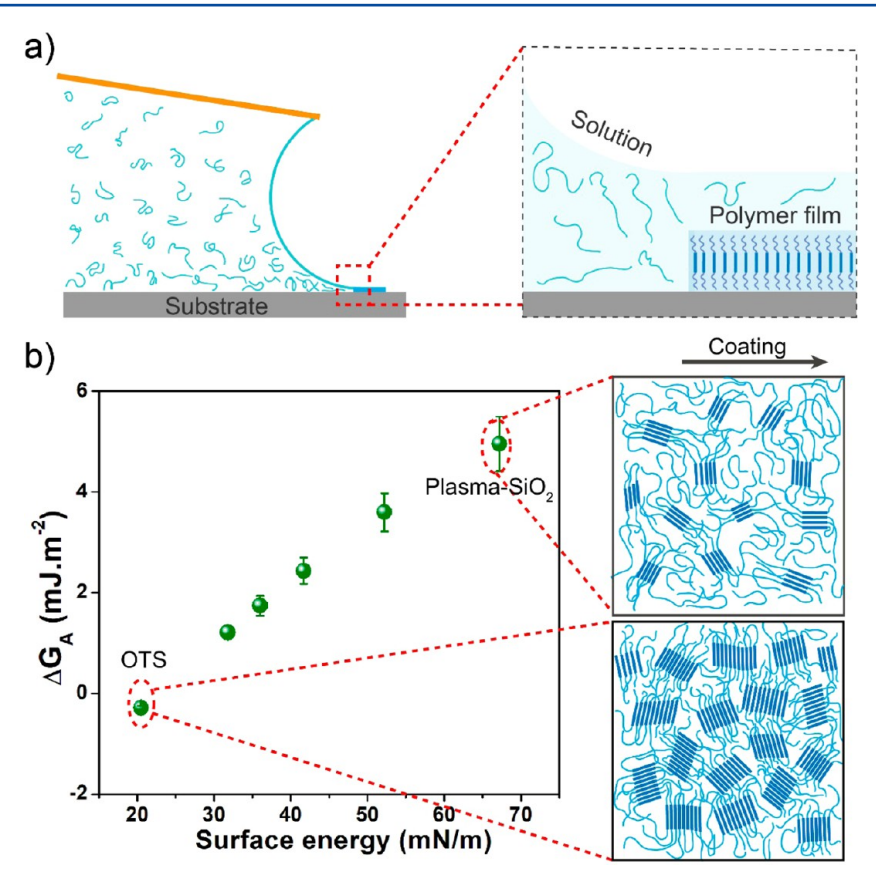


Figure 6. Free energy modeling of surface-energy-dependent excess free energy per surface area, ΔG_A . (a) Schematic of the conjugated polymer crystallization process during meniscus-guided coating. (b) Substrate surface energy dependent $\Delta G_{\rm A}$ and illustration of thin film morphology (inplane) comparing OTS and plasma-treated substrates. Alkyl chains are omitted from the illustration to highlight the change in crystallite domain size, degree of crystallinity, and alignment.

I

trapping and release, concurrent electron and hole injection, and/or field-dependent contact resistance. 76-79 We calculated mobilities in both low and high gate voltage regions (Figure S10) and observed similar trend as in the case of TGTC devices, but more dramatic change in mobility values across substrate surface energies. From OTS to plasma-treated substrate, the mobility dropped by 3 orders of magnitude (Table S3), which we attribute to a compounded effect of deteriorated thin film morphology and increased interfacial trap density.^{29,78,80} Increased interfacial trap density on high surface energy substrates also manifested in significantly increased threshold voltage (Table S3). This example reaffirms the critical importance of interfacial properties to charge transport in organic thin film transistor devices.

3.4. Free Energy Model for Heterogeneous Nucleation in Thin Film Geometry. All our morphological characterizations indicated that decreasing the substrate surface energy significantly enhances the polymer thin film degree of crystallinity. We believe that enhanced in-plane alignment can also be attributed to expedited crystallization shown in our previous work. 10 Based on these observations, we hypothesize that surface energies alter the thin film morphology by modulating the free energy barrier to heterogeneous nucleation. Compared to small molecules, heterogeneous nucleation of polymers is much less understood, particularly for conjugated polymers and crystallization from solution. Hoffman-Lauritzen (HL) theory⁸¹ and its modified forms have provided a framework for the crystal growth of chain-folded flexible polymers. However, rigid donor—acceptor conjugated polymers

exhibit distinct crystallization behavior from flexible polymers, such as the formation of 1D rod-like aggregates (vs 2D lamellae), absence of chain folding in some cases, and even small-molecule-like growth on nucleation templates. 10,19,82,83 Given these essential differences from those described by existing polymer crystallization theory, we choose to develop the relationship between the substrate surface energy and the heterogeneous nucleation barrier under a more general framework based on the classical nucleation theory. 42 We developed the free energy model specifically considering the thin film geometry, summarized below.

The total free energy change to nucleation ($\Delta G_{\text{Nucleation}}$) is generally expressed as

$$\Delta G_{\text{Nucleation}} = -V\Delta G_{\text{V}} + A\Delta G_{\text{A}}$$
 (3)

wherein $\Delta G_{\rm V}$ is the excess free energy per volume between bulk solid and solvated solute, which provides the driving force for nucleation, and ΔG_A is the excess free energy per surface area between the surface and the bulk of the nucleus, which is the penalty to forming a nucleus. In the case of heterogeneous nucleation, ΔG_A depends on the pairwise interfacial free energies between nucleus, substrate, and solvent ($\gamma_{ ext{substrate-solvent}}$) $\gamma_{
m polymer-solvent}, \gamma_{
m substrate-polymer}$), and is therefore highly sensitive to substrate surface energy. On the other hand, $\Delta G_{
m V}$ is independent of the substrate. Therefore, we only consider the penalty term, ΔG_A from now on. For the thin film case, when a 2D nucleus forms on the substrate (with contact area A) from a dilute solution, the changes in interfacial free energies of the system $(A\Delta G_A)$ are brought by the removal of the substrate-

DOI: 10.1021/acs.langmuir.7b02807 Langmuir XXXX, XXX, XXX—XXX

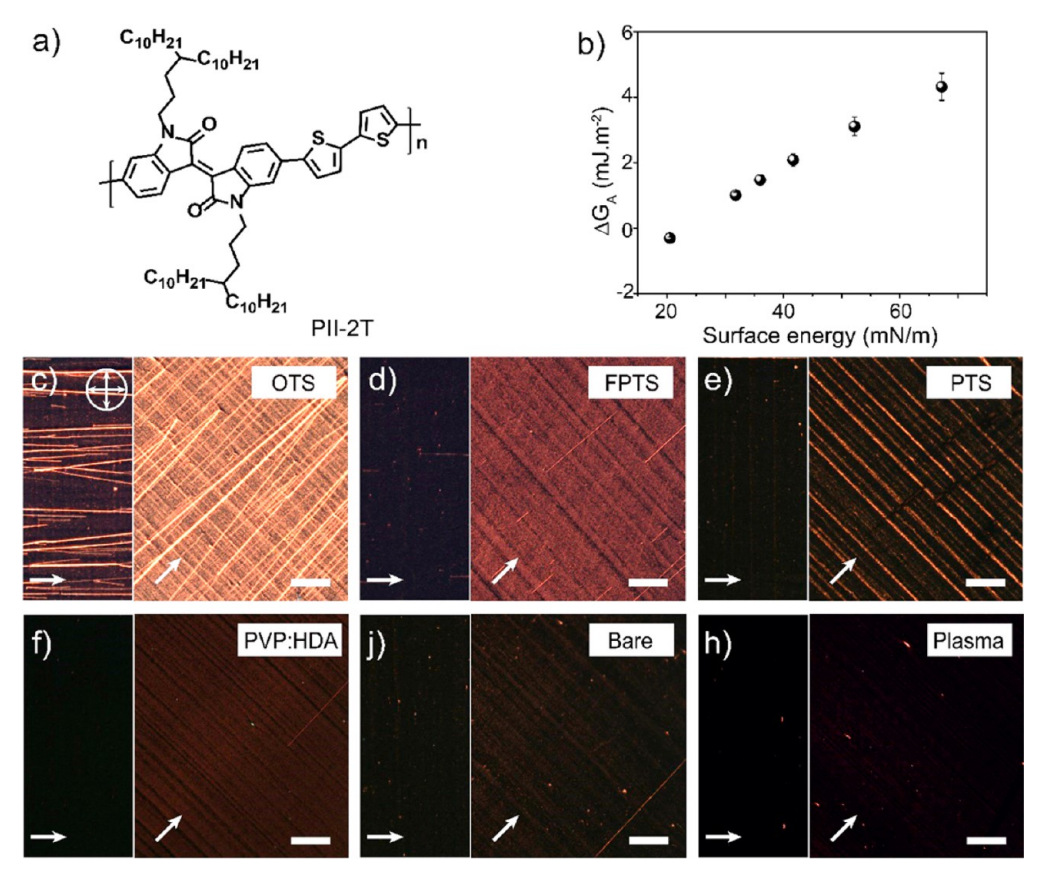


Figure 7. Dependence of PII-2T thin film morphology on substrate surface energy. (a) Molecular structure and (b) Calculated excess free energy change per surface area ΔG_A as a function of substrate surface energy for PII-2T. The solvent is chloroform. (c-h) Cross-polarized optical microscopy images of meniscus-guided coated PII-2T films on (c) OTS, (d) FPTS, (e) PTS, (f) PVP:HDA, (g) bare, and (h) plasma-treated Si/SiO₂ substrate. Scale bar: 100 μ m. The arrows indicate the coating direction.

solvent interface $(-A\gamma_{\text{substrate-solvent}})$ and the creation of two new interfaces, solvent—polymer and polymer—substrate interfaces $(A\gamma_{\text{polymer-solvent}} + A\gamma_{\text{substrate-polymer}})$. Note that the contact areas between all three pairs are equivalent for the thin film geometry. Therefore,

$$\Delta G_{A} = \gamma_{\text{polymer-solvent}} + \gamma_{\text{substrate-polymer}} - \gamma_{\text{substrate-solvent}}$$
(4)

The three interfacial free energies in eq 4 can be calculated from experimentally measured surface energies based on the equation-of-state approach introduced earlier. So Substituting Equation S3 into eq 4 and combining terms yields

$$\Delta G_{A} = 2\left[\gamma_{\text{polymer}} - \sqrt{\gamma_{\text{solvent}}\gamma_{\text{polymer}}} \left(1 - \beta(\gamma_{\text{solvent}} - \gamma_{\text{polymer}})^{2}\right) - \sqrt{\gamma_{\text{substrate}}\gamma_{\text{polymer}}} \left(1 - \beta(\gamma_{\text{substrate}} - \gamma_{\text{polymer}})^{2}\right) + \sqrt{\gamma_{\text{substrate}}\gamma_{\text{solvent}}} \left(1 - \beta(\gamma_{\text{substrate}} - \gamma_{\text{solvent}})^{2}\right)\right]$$
(5)

where γ_i is interfacial free energy between component i and air (or surface energy). Note that $\gamma_{\rm polymer}$ (DPP2T-TT surface energy) is estimated to be 22.6 \pm 2.3 mN/m (Figure S11), in a similar fashion that substrates surface energies were obtained. We approximate the surface energy of the dilute solution as that of the solvent chloroform ($\gamma_{\rm solvent}$), which is 26.7 mN/m. Figure 6 shows the dependence of $\Delta G_{\rm A}$ on the substrate surface energy: the lower the substrate surface energy, the lower the $\Delta G_{\rm A}$ and therefore the free energy barrier to nucleation. This prediction is consistent with our morphological characterizations that lower substrate surface energy enhanced the

degree of crystallinity in the polymer thin films. This effect could be comprehended from the perspective of intermolecular interactions as well. Due to the edge-on orientation of DPP2T-TT across all substrates (Figure 4), higher interactions are expected between DPP2T-TT alkyl chains and OTS alkyl chains than with other substrate chemistries studied. This favorable interaction between DPP2T-TT and OTS is manifested as low interfacial free energies between the two surfaces, driving down the nucleation penalty ΔG_A . We note that the model, however, is not able to predict the morphology dependence on surface energy quantitatively, despite matching of trends qualitatively. For instance, the abrupt morphology change from PTS to PVP:HDA is not predicted by our model. Other factors, such as surface-energy-dependent domain growth rate, and the coupling of polymer crystallization with solvent evaporation and fluid flow may also play important roles in defining the final morphology.1

3.5. Validating Model Generality. To validate the generality of our methodology, we show that our model is not limited to the deposition technique nor the choice of the conjugated polymer. This work primarily focused on meniscusguided coating considering that the technique is highly controllable and tunable, enables the deposition of aligned OSC thin films and mimics the physics of roll-to-roll printers for large scale manufacturing. We further tested spin-coated DPP2T-TT thin films on various substrates to verify that our model prediction is independent of the deposition method applied. Using an on-the-fly dispensing method, ⁴⁶ we spin-coated DPP2T-TT thin films with controlled thickness of ~30

nm (see Experimental section). As expected, the crystallinity of the spin-coated films also followed the trend predicted by the free energy model, inferred from C-POM images (Figure S12).

Furthermore, we tested another solution processable semiconducting polymer, PII-2T, featuring an isoindigo acceptor copolymerized with a bithiophene donor (Figure 7a). PII-2T surface energy was estimated to be $23.1 \pm 2.0 \text{ mN/m}$ (Figure S13). We calculated the excess free energy change per surface area (ΔG_A) as a function of substrate surface energy for PII-2T nucleation from its chloroform solution, and obtained the same trend as the case of DPP2T-TT given their similar surface energy and the same solvent, substrates used (Figure 7b). The model predicted that lower substrate surface energy would lead to lower free energy barrier to 2D nucleation from solution. Indeed, the experimental trend agreed with the trend predicted from the calculated ΔG_A values. Figures 7c-h compare the morphology of PII-2T thin films prepared by meniscus-guided coating on various substrates. The birefringence of the C-POM images dramatically increased by decreasing substrate surface energy. These results suggest that the principles we outlined for surface-energy-directed polymer crystallization can potentially be applied to other OSC systems and solution deposition techniques.

CONCLUSION

In conclusion, we observed systematic modulation of morphology and charge transport properties of solution coated DPP2T-TT D-A conjugated polymer thin films by varying the substrate surface energy. The substrate surface energy was widely tuned from 20.5 to 67.2 mN/m by surface functionalization using self-assembled monolayers, polymers and plasma treatment. We analyzed the thin film morphology on various substrates using a combination of C-POM, UV-vis, AFM, and GIXD. Morphological analysis revealed increasing degree of crystallinity (by ~22%), improving molecular ordering (FWHM decreased by 14%) and higher in-plane alignment (from isotropic to GIXD dichroic ratio of 5.2) as the surface energy decreased from 67.2 to 20.5 mN/m; the most pronounced changes took place between 41.7 and 20.5 mN/m. As a result of morphology improvement, we observed one order-of-magnitude hole-mobility enhancement of DPP2T-TT organic field-effect transistors from plasma-treated substrate (67.2 mN/m) to OTS substrate (20.5 mN/m), measured in top-gate devices. When surface-chemistry-dependent interfacial trap density was further accounted for, the hole mobility modulation reached 3 orders of magnitude by varying substrate (dielectric) surface energy, measured in bottom-gate devices. These results demonstrate that the modulation of substrate surface energy is a powerful strategy for tuning polymer thin film microstructure and charge transport properties of organic semiconductor thin films.

To elucidate the mechanism, we further established a classical-nucleation-theory-based free energy model specifically for the case of thin film crystallization. The model was developed based on the hypothesis that the surface energy modulates thin film morphology by altering the free energy barrier to heterogeneous nucleation. Our model predicted that lower substrate surface energy led to reduced surface excess free energy (nucleation penalty), thereby reducing the free energy barrier to nucleation. This prediction is qualitatively in line with the surface-energy-dependent thin film morphology observed. Enabled by this model, we propose the following mechanistic picture: low substrate surface energy better matches with the

low surface energy of crystallizing polymers with the inert alkyl chain facing the substrate, thereby reduces polymer nucleation barrier on the substrate, expedites nucleation and leaves longer time for growth and reorientation in the coating flow within the fixed time frame of solution coating. Resultantly, films coated on lower energy substrate have higher degree of crystallinity and better alignment. On the other hand, we note that change of polymer systems and solvents may completely alter the surface energy-morphology relationship. We believe that coupled effect of all three components, solute, solvent, and substrate, determines the nucleation barrier in surface-induced crystallization, implied in our model. Our methodology and mechanistic understanding have broad implications, given the importance of surface-induced crystallization across many disciplines. Furthermore, our model can potentially be used for rational selection of solvent and substrate for a given solute to promote thin film crystallization and to enhance solid-state properties.

ASSOCIATED CONTENT

S Supporting Information

The Supporting Information is available free of charge on the ACS Publications website at DOI: 10.1021/acs.langmuir.7b02807.

Surface energy determination, surface morphology (AFM), GIXD and UV-vis analysis, OFET characteristics, C-POM of spin-coated films, and surface energy of DPP2T-TT and PII-2T thin films (PDF)

AUTHOR INFORMATION

Corresponding Author

*E-mail: yingdiao@illinois.edu.

ORCID ®

Jianguo Mei: 0000-0002-5743-2715 Ying Diao: 0000-0002-8984-0051

Author Contributions

These authors contributed equally to this work.

Notes

The authors declare no competing financial interest.

ACKNOWLEDGMENTS

This research was financially supported by the startup funds of University of Illinois. Y.D. gratefully acknowledges partial support by the National Science Foundation, Division of Materials Research under grant number #1641854. J.M. acknowledges the financial support from Office of Naval Research Young Investigator Program (ONR YIP), award number N00014-16-1-2551. This research used resources of the Advanced Photon Source, a U.S. Department of Energy (DOE) Office of Science User Facility operated for the DOE Office of Science by Argonne National Laboratory under Contract No. DE-AC02-06CH11357. Thanks also to Dr. Chong-an Di of Institute of Chemistry the Chinese Academy of Sciences and Beijing National Laboratory for Molecular Sciences for assistance with device studies. Part of this work was conducted in the Frederick Seitz Materials Research Laboratory Central Facilities, University of Illinois.

REFERENCES

(1) McCulloch, I.; Heeney, M.; Bailey, C.; Genevicius, K.; Macdonald, I.; Shkunov, M.; Sparrowe, D.; Tierney, S.; Wagner, R.;

Zhang, W.; Chabinyc, M. L.; Kline, R. J.; McGehee, M. D.; Toney, M. F. Liquid-crystalline semiconducting polymers with high charge-carrier mobility. *Nat. Mater.* **2006**, *5*, 328–333.

- (2) Diao, Y.; Zhou, Y.; Kurosawa, T.; Shaw, L.; Wang, C.; Park, S.; Guo, Y.; Reinspach, J. A.; Gu, K.; Gu, X.; Tee, B. C.; Pang, C.; Yan, H.; Zhao, D.; Toney, M. F.; Mannsfeld, S. C.; Bao, Z. Flow-enhanced solution printing of all-polymer solar cells. *Nat. Commun.* **2015**, *6*, 7955.
- (3) Noriega, R.; Rivnay, J.; Vandewal, K.; Koch, F. P.; Stingelin, N.; Smith, P.; Toney, M. F.; Salleo, A. A general relationship between disorder, aggregation and charge transport in conjugated polymers. *Nat. Mater.* **2013**, *12*, 1038–1044.
- (4) Giri, G.; Verploegen, E.; Mannsfeld, S. C.; Atahan-Evrenk, S.; Kim, D. H.; Lee, S. Y.; Becerril, H. A.; Aspuru-Guzik, A.; Toney, M. F.; Bao, Z. Tuning charge transport in solution-sheared organic semiconductors using lattice strain. *Nature* **2011**, *480*, 504–508.
- (5) Qu, G.; Zhao, X.; Newbloom, G. M.; Zhang, F. J.; Mohammadi, E.; Strzalka, J. W.; Pozzo, L. D.; Mei, J.; Diao, Y. Understanding interfacial alignment in solution coated conjugated polymer thin films. ACS Appl. Mater. Interfaces 2017, 9, 27863.
- (6) Schott, S.; Gann, E.; Thomsen, L.; Jung, S. H.; Lee, J. K.; McNeill, C. R.; Sirringhaus, H. Charge-transport anisotropy in a uniaxially aligned diketopyrrolopyrrole-based copolymer. *Adv. Mater.* **2015**, *27*, 7356–7364.
- (7) Zhang, F. J.; Dai, X.; Zhu, W.; Chung, H.; Diao, Y. Large modulation of charge carrier mobility in doped nanoporous organic transistors. *Adv. Mater.* **2017**, *29*, 1700411.
- (8) Tseng, H. R.; Ying, L.; Hsu, B. B.; Perez, L. A.; Takacs, C. J.; Bazan, G. C.; Heeger, A. J. High mobility field effect transistors based on macroscopically oriented regioregular copolymers. *Nano Lett.* **2012**, *12*, *6353*–*6357*.
- (9) Bucella, S. G.; Luzio, A.; Gann, E.; Thomsen, L.; McNeill, C. R.; Pace, G.; Perinot, A.; Chen, Z.; Facchetti, A.; Caironi, M. Macroscopic and high-throughput printing of aligned nanostructured polymer semiconductors for MHz large-area electronics. *Nat. Commun.* **2015**, *6*, 8394.
- (10) Mohammadi, E.; Zhao, C. K.; Meng, Y. F.; Qu, G.; Zhang, F. J.; Zhao, X. K.; Mei, J. G.; Zuo, J.-M.; Shukla, D.; Diao, Y. Dynamic-template-directed multiscale assembly for large-area coating of highly-aligned conjugated polymer thin films. *Nat. Commun.* **2017**, *8*, 16070.
- (11) Diao, Y.; Tee, B. C.; Giri, G.; Xu, J.; Kim, D. H.; Becerril, H. A.; Stoltenberg, R. M.; Lee, T. H.; Xue, G.; Mannsfeld, S. C.; Bao, Z. Solution coating of large-area organic semiconductor thin films with aligned single-crystalline domains. *Nat. Mater.* **2013**, *12*, 665–671.
- (12) Dong, H.; Hu, W. Multilevel investigation of charge transport in conjugated polymers. *Acc. Chem. Res.* **2016**, *49*, 2435–2443.
- (13) Hiszpanski, A. M.; Loo, Y.-L. Directing the film structure of organic semiconductors via post-deposition processing for transistor and solar cell applications. *Energy Environ. Sci.* **2014**, *7*, 592–608.
- (14) Diao, Y.; Shaw, L.; Bao, Z.; Mannsfeld, S. C. B. Morphology control strategies for solution-processed organic semiconductor thin films. *Energy Environ. Sci.* **2014**, *7*, 2145–2159.
- (15) Qu, G.; Kwok, J. J.; Diao, Y. Flow-directed crystallization for printed electronics. Acc. Chem. Res. 2016, 49, 2756–2764.
- (16) Lee, S. S.; Loo, Y. L. Structural complexities in the active layers of organic electronics. *Annu. Rev. Chem. Biomol. Eng.* **2010**, *1*, 59–78.
- (17) Mei, J.; Diao, Y.; Appleton, A. L.; Fang, L.; Bao, Z. Integrated materials design of organic semiconductors for field-effect transistors. *J. Am. Chem. Soc.* **2013**, *135*, 6724–6746.
- (18) Chung, H.; Diao, Y. Polymorphism as an emerging design strategy for high performance organic electronics. *J. Mater. Chem. C* **2016**, *4*, 3915–3933.
- (19) Wang, H.; Xu, Y.; Yu, X.; Xing, R.; Liu, J.; Han, Y. Structure and morphology control in thin films of conjugated polymers for an improved charge transport. *Polymers* **2013**, *5*, 1272–1324.
- (20) Yao, Y.; Dong, H.; Hu, W. Charge transport in organic and polymeric semiconductors for flexible and stretchable devices. *Adv. Mater.* **2016**, 28, 4513–4523.

(21) Lim, J. A.; Liu, F.; Ferdous, S.; Muthukumar, M.; Briseno, A. L. Polymer semiconductor crystals. *Mater. Today* **2010**, *13*, 14–24.

- (22) Liu, S.; Wang, W. M.; Briseno, A. L.; Mannsfeld, S. C. B.; Bao, Z. Controlled deposition of crystalline oganic semiconductors for field-effect-transistor applications. *Adv. Mater.* **2009**, *21*, 1217–1232.
- (23) Shao, W.; Dong, H.; Jiang, L.; Hu, W. Morphology control for high performance organic thin film transistors. *Chem. Sci.* **2011**, *2*, 590–600.
- (24) Al-Mahboob, A.; Fujikawa, Y.; Sakurai, T.; Sadowski, J. T. Realtime microscopy of reorientation driven nucleation and growth in pentacene thin films on silicon dioxide. *Adv. Funct. Mater.* **2013**, 23, 2653–2660.
- (25) Jones, A. O. F.; Chattopadhyay, B.; Geerts, Y. H.; Resel, R. Substrate-induced and thin-film phases: Polymorphism of organic materials on surfaces. *Adv. Funct. Mater.* **2016**, *26*, 2233–2255.
- (26) Briseno, A. L.; Aizenberg, J.; Han, Y. J.; Penkala, R. A.; Moon, H.; Lovinger, A. J.; Kloc, C.; Bao, Z. Patterned growth of large oriented organic semiconductor single crystals on self-assembled monolayer templates. *J. Am. Chem. Soc.* **2005**, *127*, 12164–12165.
- (27) Ji, D.; Xu, X.; Jiang, L.; Amirjalayer, S.; Jiang, L.; Zhen, Y.; Zou, Y.; Yao, Y.; Dong, H.; Yu, J.; Fuchs, H.; Hu, W. Surface polarity and self-structured nanogrooves collaboratively oriented molecular packing for high crystallinity toward efficient charge transport. *J. Am. Chem. Soc.* 2017, 139, 2734–2740.
- (28) Lee, W. H.; Park, J.; Sim, S. H.; Lim, S.; Kim, K. S.; Hong, B. H.; Cho, K. Surface-directed molecular assembly of pentacene on monolayer graphene for high-performance organic transistors. *J. Am. Chem. Soc.* **2011**, *133*, 4447–4454.
- (29) Lee, W. H.; Cho, J. H.; Cho, K. Control of mesoscale and nanoscale ordering of organic semiconductors at the gate dielectric/semiconductor interface for organic transistors. *J. Mater. Chem.* **2010**, 20, 2549.
- (30) Xiao, M.; Jasensky, J.; Zhang, X.; Li, Y.; Pichan, C.; Lu, X.; Chen, Z. Influence of the side chain and substrate on polythiophene thin film surface, bulk, and buried interfacial structures. *Phys. Chem. Chem. Phys.* **2016**, *18*, 22089–22099.
- (31) Virkar, A. A.; Mannsfeld, S. C. B.; Bao, Z. Energetics and stability of pentacene thin films on amorphous and crystalline octadecylsilane modified surfaces. *J. Mater. Chem.* **2010**, *20*, 2664.
- (32) Kang, B.; Jang, M.; Chung, Y.; Kim, H.; Kwak, S. K.; Oh, J. H.; Cho, K. Enhancing 2D growth of organic semiconductor thin films with macroporous structures via a small-molecule heterointerface. *Nat. Commun.* **2014**, *5*, 4752.
- (33) Ribič, P. R.; Kalihari, V.; Frisbie, C. D.; Bratina, G. Growth of ultrathin pentacene films on polymeric substrates. *Phys. Rev. B: Condens. Matter Mater. Phys.* **2009**, *80*, 115307.
- (34) Na, J. Y.; Kang, B.; Lee, S. G.; Cho, K.; Park, Y. D. Surface-mediated solidification of a semiconducting polymer during time-controlled spin-coating. *ACS Appl. Mater. Interfaces* **2017**, *9*, 9871–9879.
- (35) Joseph Kline, R.; McGehee, M. D.; Toney, M. F. Highly oriented crystals at the buried interface in polythiophene thin-film transistors. *Nat. Mater.* **2006**, *5*, 222–228.
- (36) Kim, D. H.; Park, Y. D.; Jang, Y.; Yang, H.; Kim, Y. H.; Han, J. I.; Moon, D. G.; Park, S.; Chang, T.; Chang, C.; Joo, M.; Ryu, C. Y.; Cho, K. Enhancement of field-effect mobility due to surface-mediated molecular ordering in regioregular polythiophene thin film transistors. *Adv. Funct. Mater.* **2005**, *15*, 77–82.
- (37) Kim, D. H.; Jang, Y.; Park, Y. D.; Cho, K. Surface-induced conformational changes in poly(3-hexylthiophene) monolayer films. *Langmuir* **2005**, *21*, 3203–3206.
- (38) Umeda, T.; Kumaki, D.; Tokito, S. Surface-energy-dependent field-effect mobilities up to 1cm²/V s for polymer thin-film transistor. *J. Appl. Phys.* **2009**, *105*, 024516.
- (39) Anglin, T. C.; Speros, J. C.; Massari, A. M. Interfacial ring orientation in polythiophene field-effect transistors on functionalized dielectrics. *J. Phys. Chem. C* **2011**, *115*, 16027–16036.

(40) Lee, S. S.; Tang, S. B.; Smilgies, D. M.; Woll, A. R.; Loth, M. A.; Mativetsky, J. M.; Anthony, J. E.; Loo, Y. L. Guiding crystallization around bends and sharp corners. *Adv. Mater.* **2012**, *24*, 2692–2698.

- (41) Diao, Y.; Myerson, A. S.; Hatton, T. A.; Trout, B. L. Surface design for controlled crystallization: the role of surface chemistry and nanoscale pores in heterogeneous nucleation. *Langmuir* **2011**, 27, 5324–5334.
- (42) Mullin, J. W. Crystallization; Butterworth-Heinemann: London, 2001.
- (43) Li, Y.; Singh, S. P.; Sonar, P. A high mobility P-type DPP-thieno[3,2-b]thiophene copolymer for organic thin-film transistors. *Adv. Mater.* **2010**, *22*, 4862–4866.
- (44) Xue, G.; Zhao, X.; Qu, G.; Xu, T.; Gumyusenge, A.; Zhang, Z.; Zhao, Y.; Diao, Y.; Li, H.; Mei, J. Symmetry breaking in side chains leading to mixed orientations and improved charge transport in isoindigo-alt-bithiophene based polymer thin films. ACS Appl. Mater. Interfaces 2017, 9, 25426–25433.
- (45) Zhang, F. J.; Qu, G.; Mohammadi, E.; Mei, J.; Diao, Y. Solution-processed nanoporous organic semiconductor thin films: Toward health and environmental monitoring of volatile markers. *Adv. Funct. Mater.* **2017**, 27, 1701117.
- (46) Zhang, F. J.; Di, C. A.; Berdunov, N.; Hu, Y. B.; Gao, X. K.; Meng, Q.; Sirringhaus, H.; Zhu, D. B. Ultrathin Film Organic Transistors: Precise Control of Semiconductor Thickness via Spin-Coating. *Adv. Mater.* **2013**, 25, 1401–1407.
- (47) Jiang, Z.; Li, X.; Strzalka, J.; Sprung, M.; Sun, T.; Sandy, A. R.; Narayanan, S.; Lee, D. R.; Wang, J. The dedicated high-resolution grazing-incidence X-ray scattering beamline 8-ID-E at the Advanced Photon Source. *J. Synchrotron Radiat.* **2012**, *19*, 627–636.
- (48) Jiang, Z. GIXSGUI: a MATLAB toolbox for grazing-incidence X-ray scattering data visualization and reduction, and indexing of buried three-dimensional periodic nanostructured films. *J. Appl. Crystallogr.* **2015**, *48*, 917–926.
- (49) Baker, J. L.; Jimison, L. H.; Mannsfeld, S.; Volkman, S.; Yin, S.; Subramanian, V.; Salleo, A.; Alivisatos, A. P.; Toney, M. F. Quantification of thin film crystallographic orientation using X-ray diffraction with an area detector. *Langmuir* **2010**, *26*, 9146–9151.
- (50) Fowkes, F. M. Attractive forces at interfaces. *Ind. Eng. Chem.* **1964**, *56*, 40–52.
- (51) Owens, D. K.; Wendt, R. C. Estimation of the surface free energy of polymers. J. Appl. Polym. Sci. 1969, 13, 1741–1747.
- (52) Berthelot, D. Comptes Rendus 1898, 126, 1857.
- (53) Antonow, G. N. Sur la tension superficielle à la limite de deux couches. J. Chim. Phys. Phys.-Chim. Biol. 1907, 5, 372–385.
- (54) Li, D.; Neumann, A. W. A reformulation of the equation of state for interfacial tensions. *J. Colloid Interface Sci.* **1990**, *137*, 304–307.
- (55) Israelachvili, J. N. In *Intermolecular and Surface Forces*, 3rd ed.; Academic Press: Boston, MA, 2011.
- (56) Kwok, D. Y.; Neumann, A. W. Contact angle measurement and contact angle interpretation. *Adv. Colloid Interface Sci.* **1999**, *81*, 167–249.
- (57) Young, T. An Essay on the Cohesion of Fluids. *Philos. Trans. R. Soc. London A* **1805**, *95*, 65–87.
- (58) Cheng, P.; Li, D.; Boruvka, L.; Rotenberg, Y.; Neumann, A. W. Automation of axisymmetric drop shape analysis for measurements of interfacial tensions and contact angles. *Colloids Surf.* **1990**, *43*, 151–167
- (59) Neumann, A. W. Contact angles and their temperature dependence: thermodynamic status, measurement, interpretation and application. *Adv. Colloid Interface Sci.* **1974**, *4*, 105–191.
- (60) Li, D.; Neumann, A. W. Contact angles on hydrophobic solid surfaces and their interpretation. *J. Colloid Interface Sci.* **1992**, *148*, 190–200.
- (61) Li, D.; Xie, M.; Neumann, A. W. Vapour adsorption and contact angles on hydrophobic solid surfaces. *Colloid Polym. Sci.* **1993**, *271*, 573–580.
- (62) Lim, S. C.; Kim, S. H.; Lee, J. H.; Kim, M. K.; Kim, D. J.; Zyung, T. Surface-treatment effects on organic thin-film transistors. *Synth. Met.* **2005**, *148*, 75–79.

(63) Janssen, D.; De Palma, R.; Verlaak, S.; Heremans, P.; Dehaen, W. Static solvent contact angle measurements, surface free energy and wettability determination of various self-assembled monolayers on silicon dioxide. *Thin Solid Films* **2006**, *515*, 1433–1438.

- (64) Li, Y.; Sonar, P.; Murphy, L.; Hong, W. High mobility diketopyrrolopyrrole (DPP)-based organic semiconductor materials for organic thin film transistors and photovoltaics. *Energy Environ. Sci.* **2013**, *6*, 1684–1710.
- (65) Yi, Z.; Wang, S.; Liu, Y. Design of high-mobility diketopyrrole-based pi-conjugated copolymers for organic thin-film transistors. *Adv. Mater.* **2015**, *27*, 3589–3606.
- (66) Lei, Y.; Deng, P.; Li, J.; Lin, M.; Zhu, F.; Ng, T. W.; Lee, C. S.; Ong, B. S. Solution-processed donor-acceptor polymer nanowire network semiconductors for high-performance field-effect transistors. *Sci. Rep.* **2016**, *6*, 24476.
- (67) Watanabe, S.; Inukai, K.; Mizuta, S.; Miyahara, M. T. Mechanism for stripe pattern formation on hydrophilic surfaces by using convective self-assembly. *Langmuir* **2009**, *25*, 7287–7295.
- (68) Vezie, M. S.; Few, S.; Meager, I.; Pieridou, G.; Dorling, B.; Ashraf, R. S.; Goni, A. R.; Bronstein, H.; McCulloch, I.; Hayes, S. C.; Campoy-Quiles, M.; Nelson, J. Exploring the origin of high optical absorption in conjugated polymers. *Nat. Mater.* **2016**, *15*, 746–753.
- (69) Kraus, A.; Köhler, A.; dos Santos, D. A.; Beljonne, D.; Shuai, Z.; Brédas, J. L.; Holmes, A. B.; Müllen, K.; Friend, R. H. Charge separation in localized and delocalized electronic states in polymeric semiconductors. *Nature* **1998**, *392*, 903–906.
- (70) Luzio, A.; Criante, L.; D'Innocenzo, V.; Caironi, M. Control of charge transport in a semiconducting copolymer by solvent-induced long-range order. *Sci. Rep.* **2013**, *3*, 3425.
- (71) Jimison, L. H. Understanding Microstructure and Charge Transport in Semicrystalline Polythiophenes; Stanford University: Stanford, CA, 2011.
- (72) Rivnay, J.; Mannsfeld, S. C.; Miller, C. E.; Salleo, A.; Toney, M. F. Quantitative determination of organic semiconductor microstructure from the molecular to device scale. *Chem. Rev.* **2012**, *112*, 5488–5519.
- (73) Hammond, M. R.; Kline, R. J.; Herzing, A. A.; Richter, L. J.; Germack, D. S.; Ro, H. W.; Soles, C. L.; Fischer, D. A.; Xu, T.; Yu, L.; Toney, M. F.; Delongchamp, D. M. Molecular order in high-efficiency polymer/fullerene bulk heterojunction solar cells. *ACS Nano* **2011**, *5*, 8248–8257.
- (74) Li, J.; Zhao, Y.; Tan, H. S.; Guo, Y.; Di, C. A.; Yu, G.; Liu, Y.; Lin, M.; Lim, S. H.; Zhou, Y.; Su, H.; Ong, B. S. A stable solution-processed polymer semiconductor with record high-mobility for printed transistors. *Sci. Rep.* **2012**, *2*, 754.
- (75) Chen, Z.; Lee, M. J.; Shahid Ashraf, R.; Gu, Y.; Albert-Seifried, S.; Meedom Nielsen, M.; Schroeder, B.; Anthopoulos, T. D.; Heeney, M.; McCulloch, I.; Sirringhaus, H. High-performance ambipolar diketopyrrolopyrrole-thieno[3,2-b]thiophene copolymer field-effect transistors with balanced hole and electron mobilities. *Adv. Mater.* 2012, 24, 647–652.
- (76) McCulloch, I.; Salleo, A.; Chabinyc, M. Avoid the kinks when measuring mobility. *Science* **2016**, 352, 1521–1522.
- (77) Uemura, T.; Rolin, C.; Ke, T.-H.; Fesenko, P.; Genoe, J.; Heremans, P.; Takeya, J. On the Extraction of Charge Carrier Mobility in High-Mobility Organic Transistors. *Adv. Mater.* **2016**, 28, 151–155.
- (78) Sirringhaus, H. Device physics of solution-processed organic field-effect transistors. *Adv. Mater.* **2005**, *17*, 2411–2425.
- (79) Bittle, E. G.; Basham, J. I.; Jackson, T. N.; Jurchescu, O. D.; Gundlach, D. J. *Nat. Commun.* **2016**, *7*, 10908.
- (80) Di, C. A.; Liu, Y.; Yu, G.; Zhu, D.B. Interface engineering: an effective approach toward high-performance organic field-effect transistors. *Acc. Chem. Res.* **2009**, *42*, 1573–1583.
- (81) Cheng, S. Z. D.; Lotz, B. Enthalpic and entropic origins of nucleation barriers during polymer crystallization: the Hoffman–Lauritzen theory and beyond. *Polymer* **2005**, *46*, 8662–8681.
- (82) Liu, J.; Mikhaylov, I. A.; Zou, J.; Osaka, I.; Masunov, A. E.; McCullough, R. D.; Zhai, L. Insight into how molecular structures of

Langmuir

thiophene-based conjugated polymers affect crystallization behaviors. *Polymer* **2011**, *52*, 2302–2309.

- (83) Miura, T.; Kishi, R.; Mikami, M.; Tanabe, Y. Effect of rigidity on the crystallization processes of short polymer melts. *Phys. Rev. E: Stat. Phys., Plasmas, Fluids, Relat. Interdiscip. Top.* **2001**, 63, 061807.
- (84) Green, D. W.; Perry, R. H. *Perry's Chemical Engineers' Handbook*; McGraw-Hill Professional: New York, 1999.